

Vector-FRI Recovery of Multi-Sensor Measurements

Ruiming Guo , Yongfei Li , Thierry Blu , *Fellow, IEEE*, and Hangfang Zhao 

Abstract—Thanks to lowering costs, sensors of all kinds have increasingly been used in a wide variety of disciplines and fields, facilitating the rapid development of new technologies and applications. The information of interest (e.g. source location, refractive index, etc.) gets encoded in the measured sensor data, and the key problem is then to decode this information from the sensor measurements. In many cases, sensor data exhibit sparse features—“innovations”—that typically take the form of a finite sum of sinusoids. In practice, the robust retrieval of such encoded information from multi-sensors data (array or network) is difficult due to the non-uniformity of instrument precision and noise (i.e. different across sensors). This motivates the development of a joint sparse (“vector Finite Rate of Innovation”) recovery strategy for multi-sensor data: by fitting the data to a joint parametric model, an accurate sparse recovery can be achieved, even if the noise of the sensors is non-homogenous and correlated. Although developed for one-dimensional sensor data, we show that our method is easily extended to multi-dimensional sensor measurements, e.g. direction-of-arrival data of 2D planar array and interference fringes of underwater acoustics, which provides a generic solution to these applications. A very robust and efficient algorithm is proposed, which we validate in various conditions (simulations, multiple types of real data).

Index Terms—Vector finite-rate-of-innovation (FRI), multi-sensor measurements, data fusion, multi-dimensional sparse recovery, high-resolution, model-fitting.

I. INTRODUCTION

Sparse Signal Recovery—Nowadays, the wide availability of various cheap sensors (inertia, velocity, magnetic field, acoustic, pressure, temperature, etc.) makes it possible to develop new

Manuscript received 28 November 2021; revised 25 May 2022 and 31 August 2022; accepted 31 August 2022. Date of publication 5 September 2022; date of current version 14 September 2022. The associate editor coordinating the review of this manuscript and approving it for publication was Dr. Hassan Mansour. This work was supported in part by the National Natural Science Foundation of China under Grant 62071429 and in part by the National Key R&D Program of China under Grants 2016YFC and 1400100. (*Corresponding author: Ruiming Guo.*)

Ruiming Guo and Thierry Blu are with the Department of Electronic Engineering, The Chinese University of Hong Kong, Hong Kong 999077, Hong Kong (e-mail: 1155100873@link.cuhk.edu.hk; thierry.blu@m4x.org).

Yongfei Li is with the College of Information Science and Electronic Engineering, Zhejiang University, Hangzhou City, Zhejiang Province 310007, China (e-mail: liyongfei@zju.edu.cn).

Hangfang Zhao is with the College of Information Science and Electronic Engineering, Zhejiang University, Hangzhou City, Zhejiang Province 310007, China, with the Laboratory of Ocean Observation-Imaging Testbed of Zhejiang Province, Zhoushan City, Zhejiang Province 316021, China, with the Engineering Research Center of Oceanic Sensing Technology and Equipment, Ministry of Education, Zhoushan City, Zhejiang Province 316021, China, and also with the State Key Laboratory of Fluid Power and Mechatronic Systems, Zhejiang University, Hangzhou City, Zhejiang Province 310007, China (e-mail: hfhzhao@zju.edu.cn).

The code is available at <http://www.ee.cuhk.edu.hk/~tblu/vectorFRI/>.

This article has supplementary downloadable material available at <https://doi.org/10.1109/TSP.2022.3204402>, provided by the authors.

Digital Object Identifier 10.1109/TSP.2022.3204402

technologies and applications. The sensors are deployed in many places, and provide large amounts of data of all kinds. For example, the sensors installed on parcels enable real-time tracking in express delivery [1]; the sonar systems fitted on ships help identify the underwater sediment composition by analyzing the reflected echo [2].

The information of interest (e.g. direction of the source, properties of the medium/material) gets encoded in the sensor data received, and the inverse problem is then to decode this physical information from the acquired sensor data. The key observation is that, in many cases, the physical properties measured are characterized by a few parameters (innovations), which suggests exploiting the principle of sparsity as a reconstruction constraint. Fig. 1 shows several practical application examples. More specifically, these signals have few degrees of freedom (i.e., “innovations”) represented by a sparse parametric model [3], [4], [5]. Usually, these sparse signals are or can be transformed into a finite sum of sinusoids, hence converting the sparse signal recovery into frequency estimation [6], [7], [8], [9], [10], [11], [12]. From a technical point of view, this becomes a classical high-resolution frequency estimation problem, which is encountered in many applications [13], [14], [15], [16], [17].

Joint Frequency Estimation—Although high-resolution frequency estimation techniques have achieved great success in some application scenarios, there are still unresolved issues in practice. A first challenge is joint frequency retrieval from multi-sensor measurements. When measuring a physical phenomenon, two possible cases occur frequently in real data acquisition:

- 1) sensors are of the same type, but with different configurations. Usually, real sensors deployed in an array or system have a different measurement precision and noise level [18], [19], [20], [21].
- 2) sensors are of distinct types. For example, a person’s respiratory rate can be evaluated by fusing the data measured from an accelerometer, a pulse oximeter, and a sphygmomanometer [22], [23], [24]; in structural health monitoring, the natural frequency of the bridge/building can be estimated by exploiting jointly data from various sensors: accelerometer, ultrasonic sensor, acoustic emission sensor, eddy current sensor, laser Doppler vibrometer (LDVs), and strain gauge. [25], [26], [27], [28], [29].

In these circumstances, multiple sensor measurements which intrinsically share the same sinusoidal components are acquired. In practice, the most common operation is to directly or indirectly average the estimation results obtained from each individual sensor data, but this is not robust enough, nor

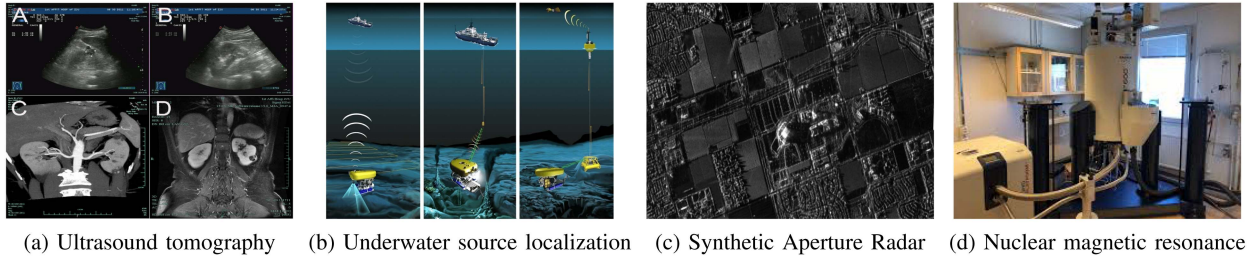


Fig. 1. A wide range of practical applications involving the acquisition of reconstruction of sparse signals.

sample-efficient. As a consequence, the final resolution provided by these frequency estimation techniques is unsatisfactory, as it largely limits the precision and reliability in many cases [30], [31], [32].

Another challenge to joint frequency retrieval is the noise that distorts the sensor measurements. It is usually assumed to be additive white Gaussian noise (i.e. AWGN) or independent and identically distributed white noise in most of the existing frequency estimation approaches (e.g. MUSIC [33], [34], ESPRIT [35], [36], matrix pencil [37], [38], compressive sensing [39], [40], etc.). However, this noise assumption is at odds with reality, where the actual measurement noise is very often correlated and colored [41], [42], [43], [44]. This model mismatch restricts the scope of applications and results in limited resolution improvement brought by frequency estimation.

Finally, a significant difficulty in joint frequency estimation is the extension to multi-dimensional sensor data, such as 2D seismic interferograms [45] and 3D holograms [46]. The lack of general joint estimation approaches has led to the design of specific ad hoc multidimensional frequency estimation techniques in different disciplines. Unfortunately, the sensor data are not optimally utilized for joint frequency retrieval, leading to limited resolution and precision on the final reconstruction result [47], [48].

Our contribution — In this paper, we propose an efficient and robust grid-less algorithm that is able to retrieve the common frequencies of data acquired by multiple sensors: Vector FRI (“Finite Rate of Innovation”). Instead of specifying a stochastic noise model, we merely opt for a single quantity—“MSE budget”—to describe *arbitrary* data corruption, (e.g. deterministic interference, non-white, correlated, non-stationary, etc.). This allows us to accurately retrieve the information from diverse multi-sensor measurements contaminated by *arbitrary* noise.

Our processing consists in performing the inverse DFT of the multi-sensor sinusoidal measurements to obtain sparse signals that are then fitted to a finite sum of Dirichlet sinc kernels. The key idea is that *any* such sum that fits the data as well or better than some known mean-square error—a predefined “MSE budget”—is a valid solution to our problem; i.e., we do not try to find the best fit. Hence, this processing does not make any statistical assumption about noise, but for its MSE to be no larger than the MSE budget: our fitted parametric model is as close (or better) to the noisy data as the (hypothetical) ground-truth is. Moreover, the MSE criterion also provides a natural way of determining the order of the model: the smallest number of

innovations/sinusoids for which the fitting MSE is still not larger than the MSE budget.

We demonstrate that our Vector-FRI algorithm can robustly process different types of sensor data, which we validate in various conditions (see Section IV). Moreover, our algorithm can be directly generalized to multi-dimensional sensor measurements, enjoying efficient implementation, strong robustness and high accuracy (see Section V). Suitable application areas range from 3D point source localization, direction-of-arrival estimation for 3D sensor array, image enhancement for fluorescence microscopy, to phase recovery from interference fringes, which is likely to help achieve high-quality signal recovery (i.e. super-resolution), and extensive adaptability to real data and hardware.

The contribution of this work can be summarized as follows:

- 1) An efficient and robust grid-less algorithm for joint sparse recovery of diverse multi-sensor measurements in the presence of *arbitrary* noise (see theory in Section II, algorithmics in Section III, and validation with simulated data in Section IV).
- 2) An extension to multi-dimensional data (see Section IV-C and Figures in the supplementary materials).
- 3) A validation with real data from two acoustic applications (see Section V).

II. VECTOR-FRI APPROXIMATION

In many application scenarios, data are measured and collected in a duration of time using sensor network or arrays. The goal is to jointly exploit these multi-sensor measurements and retrieve the encoded physical information of interest (e.g. direction of the source, properties of the medium/material, refractive index, etc.).

A. Signal Model

Consider an array of L sensors or network nodes, which provides a collection of 1D sinusoidal signals with the same frequencies; i.e. vector signals

$$s_{n,l} = \sum_{k=1}^K c_{k,l} e^{-j u_k n}, \quad n = 0, 1, \dots, N-1 \text{ and } l = 0, 1, \dots, L-1 \quad (1)$$

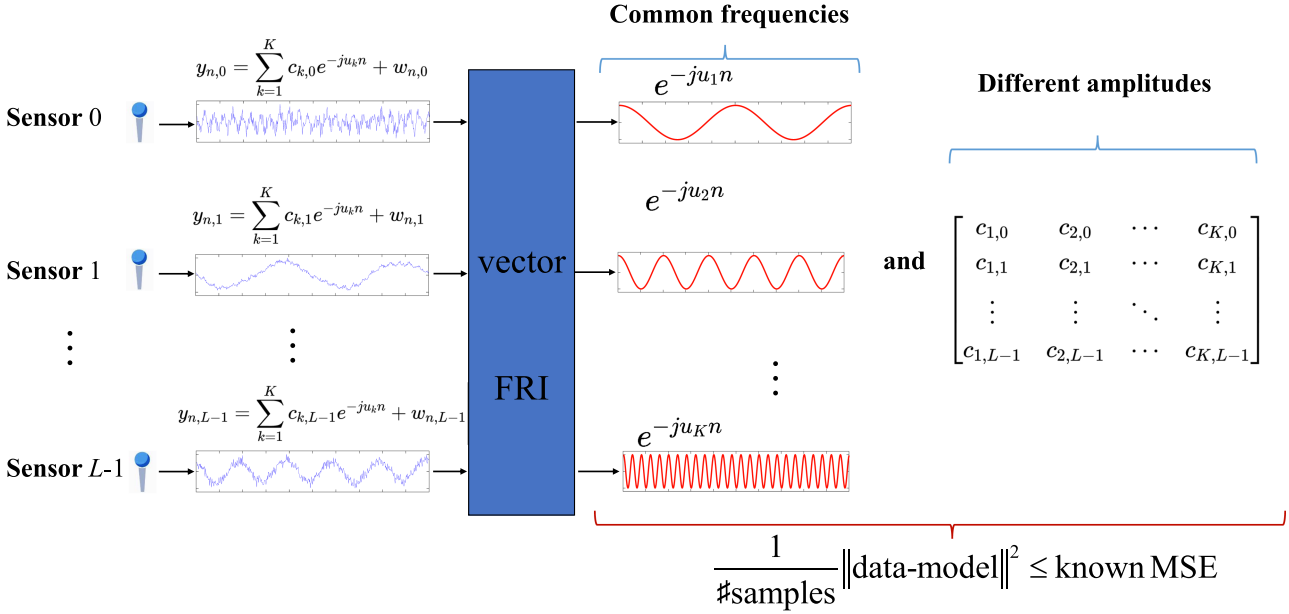


Fig. 2. Multiple sensor measurements are made up of K different complex exponentials (+noise) of the same frequencies across sensors, but different (complex) amplitudes. The goal of this paper is to retrieve these frequencies and the amplitudes of the sinusoids for each sensor.

where n is the time index, u_k is the frequency of the k -th sinusoid (common to all the L sensors), and $c_{k,l}$ is the (complex-valued) amplitude of the k -th sinusoid in the l -th sensor signal.

In noisy conditions, the sensor measurements $y_{n,l}$ can be expressed as

$$y_{n,l} = s_{n,l} + w_{n,l} \quad (2)$$

where $w_{n,l}$ denotes the noise on l -th sensor. In practice, high-resolution techniques are required as the number of samples N is limited and FFT-based techniques cannot resolve closely-located frequencies [40], [41], [48].

Note that, in various applications, we cannot usually assume that the measurement noise is white and uncorrelated between channels. However, some knowledge of the time-domain MSE of $w_{n,l}$ for each sensor should, in principle, be available (see Section II-C). A visual depiction of the problem is shown in Fig. 2.

We first briefly introduce the FRI signal model on a single sensor measurement $s_{n,l}$: the key idea is that the inverse Discrete Fourier Transform (DFT) of a sum of K sinusoids is a sum of Dirichlet sinc kernels which can, eventually, be expressed in the form of a ratio of two polynomials in $z = e^{j2\pi m/N}$ [49], [50], [51], [8]

$$\frac{1}{N} \sum_{n=0}^{N-1} s_{n,l} z^n = \frac{P_{K-1,l}(z)}{Q_K(z)} \quad (3)$$

where $P_{K-1,l}$ and Q_K are polynomials of degree $K - 1$ and K , respectively. In fact, Q_K corresponds to an annihilation filter [52], [53], the zeros of which uniquely define the frequencies u_k of the sensor signal [49].

Due to Parseval's identity, we can fit the IDFT, $x_{m,l}$, of the sensor measurements, $y_{n,l}$, with the trigonometric fraction (3), and still be ensured that we are equivalently fitting sensor data

with a sum of complex exponentials (1). Consequently, FRI approximation essentially boils down to solving the following minimization problem [49], [50]

$$\min_{Q_K, P_{K-1,l}} \sum_{m=0}^{N-1} \left| x_{m,l} - \frac{P_{K-1,l}(e^{j2\pi m/N})}{Q_K(e^{j2\pi m/N})} \right|^2 \quad (4)$$

for each sensor separately. This, however, leads to as many groups of K frequencies as there are sensors: simply averaging them would not be accurate, nor robust enough. This motivates us to develop a joint FRI recovery model for multi-sensor measurements (i.e. vector signals).

B. Vector-FRI Approximation

Notice that, the denominator Q_K of the fraction (3) is unchanged across all sensor measurements, because the frequencies u_k are the same for all the sensors. Therefore, we formulate the joint fitting problem for multi-sensor measurements as

$$\min_{Q_K, P_{K-1,l}} \sum_{l=0}^{L-1} \sum_{m=0}^{N-1} \left| x_{m,l} - \frac{P_{K-1,l}(e^{j2\pi m/N})}{Q_K(e^{j2\pi m/N})} \right|^2 \quad (5)$$

where the polynomial Q_K in the denominator is the same for all the sensors. The numerators $P_{K-1,l}$, on the other hand, differ from sensor to sensor and hence, convey the diversity and richness of the sensor measurements. Notice that, as soon as Q_K is known, the numerators $P_{K-1,l}$ are found exactly by solving a linear system of equations. Hence, (5) can be seen as an optimization problem on Q_K only.

To find a good approximation of the solution of (5), we adopt the same strategy as in [49]; i.e., we construct several candidates for the denominator Q_K , and select the one that decreases most the MSE with the multi-sensor data: as soon as the fitting error is less than a predefined MSE budget, the approximate solution

found is already sufficiently good in practice. More specifically, these candidates are found iteratively as the solution of a linear system of equations that solve the optimization problem

$$\min_{Q, P_l} \sum_{l=0}^{L-1} \sum_{m=0}^{N-1} \left| \frac{x_{m,l} Q(e^{2j\pi m/N}) - P_l(e^{2j\pi m/N})}{Q_K^{i-1}(e^{2j\pi m/N})} \right|^2 \quad (6)$$

where $i = 1, 2, \dots, i_{\max}$. Although similar in some aspects to the Sanathanan-Koerner [54] or Steiglitz-McBride [55] algorithms, our model-fitting algorithm has two important differences: firstly, we approach the problem in terms of fitting using an MSE budget. Hence, instead of looking for convergence, we stop the algorithm once the MSE budget is satisfied. Secondly, we perform *exact* model-fitting in the “sparse” domain (i.e. “frequency” domain), whereas the Steiglitz-McBride algorithm is developed and implemented in the “sinusoid” domain, using boundary conditions (typically, zero-padding) and hypotheses (i.e. causality that are inappropriate for our problem). This makes the frequency estimation obtained by using Steiglitz-McBride algorithm unreliable [56]. Changing initialization of these iterations provides more candidates. In the vast majority of the cases, 5 random initializations and $i_{\max} = 10$ are sufficient to obtain a solution that satisfies the stopping criterion (10) (see Section III-A for more details).

Having estimated the polynomials $Q_K, P_{K-1,l}$, the frequencies u_k can be obtained by computing the zeros, z_k , of the denominator

$$u_k = \text{Im}(\log(z_k)) \quad (7)$$

and the associated amplitudes can be calculated by

$$c_{k,l} = -\frac{N z_k^{-1} P_{K-1,l}(z_k)}{(1 - z_k^{-N}) Q'_K(z_k)} \quad (8)$$

for each sensor $l = 0, 1, \dots, L - 1$.

C. Vector MSE Criterion

In practical applications, the actual measurement noise is likely to be correlated (sensor-wise) and colored [41], [42], [43]. This makes it difficult to propose a general noise model suitable for most situations. In fact, the most reliable information that we have in practice is the noise margin

$$\sigma_l^2 = \frac{1}{N} \sum_{n=0}^{N-1} |w_{n,l}|^2, \quad l = 0, \dots, L - 1 \quad (9)$$

which can be obtained by pre-calibration, or from the instrument parameters, or running the algorithm of a fixed number of iterations and initializations and choosing the reconstruction that yields the minimum MSE. This motivates us to move our attention from a statistical noise model to a deterministic uncertainty of the sensor data. In other words, we only consider the deterministic noise margin (“MSE budget”) of our sensor data without imposing further assumptions. Hence, we expect that the accurate retrieval of the information conveyed by the multi-sensor signal is made possible essentially thanks to the very strong constraints of the parametric model.

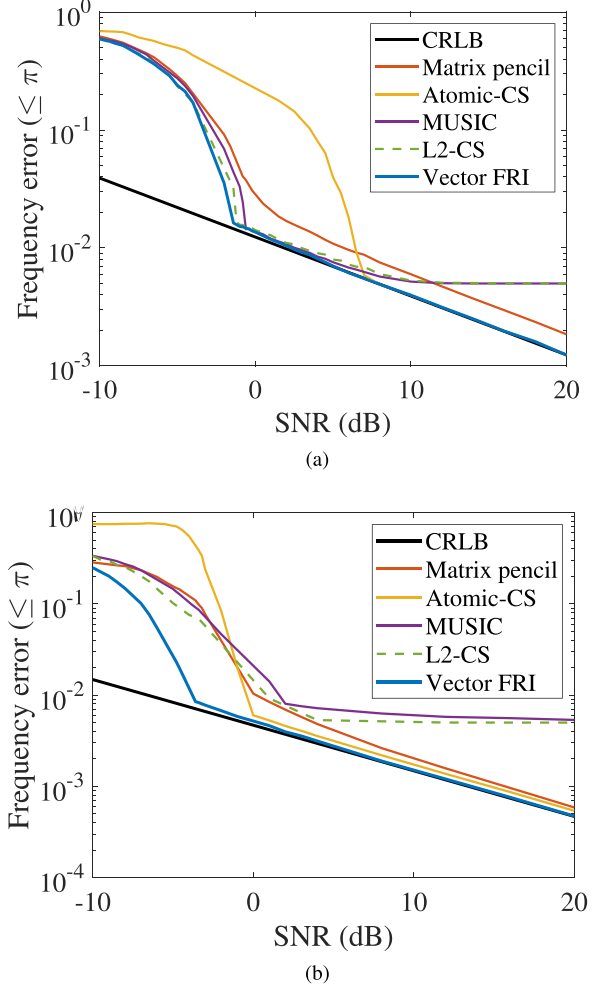


Fig. 3. Performance comparison (additive white Gaussian noise, averages over 5000 random realizations) in terms of the Cramér-Rao lower bounds (CRLB). (a) $K = 1$ sinusoid, $N = 11$ samples and $L = 3$ sensors. (b) $K = 4$ sinusoids, $N = 21$ samples and $L = 3$ sensors. Here, we compute the mean of the Cramér-Rao variances of the frequencies and compare it with the mean of the estimation variances of each algorithm.

It is inherent to this approach that any K -sinusoidal estimate that fits our samples within the MSE budget is a valid solution to our problem.

$$\text{MSE}_l \leq \sigma_l^2, \quad l = 0, \dots, L - 1 \quad (10)$$

where MSE_l is the MSE between the reconstructed signals and measurements of the l -th sensor. Clearly, we do not have the ambition to minimize the MSE defined in (6); our more modest goal is to find a valid solution, that fits our multi-sensor data up to an uncertainty characterized by σ_l^2 .

Therefore, we consider the joint FRI recovery to be successful as soon as the fitting error MSE_l is less than the corresponding MSE budget σ_l^2 for all the sensor measurements, which leads to the vector MSE criterion. Our observation in practice is that any solution that satisfies the MSE budget is sufficiently accurate—controlled accuracy on the parameters (reaching Cramér-Rao lower bounds, see Fig. 3), which can be reliably achieved by a few iterations and initializations. We demonstrate that this

vector MSE criterion guarantees the robustness and accuracy of the joint frequency retrieval, which we validate in various simulations and experiments (see Section IV and Section V).

D. Multi-Dimensional FRI Approximation

Multi-dimensional sinusoidal signals, such as hydrophone measurements from 2D planar array, optical interferometric image, and interference fringes in underwater acoustics, are ubiquitous.

Multi-dimensional FRI recovery can be seen as a Vector-FRI approximation problem by flattening the multi-dimensional signal. More specifically, vectorizing the signal along a specific dimension essentially leads to a collection of 1D signals with the same frequencies. By applying the Vector-FRI approximation for each dimension, the individual coordinates of the multi-dimensional frequencies can be accurately retrieved, albeit separately.

It is then necessary to pair these coordinates. An intuitive idea is to utilize an amplitude criterion: the modulus should be invariant across different dimensions. However, due to the approximation error, the amplitude estimation is not sufficiently robust in the presence of noise corruption, and hence, cannot be used alone for pairing purposes.

Another idea is to fit all possible sinusoids (i.e., K^D , if D is the dimension of the measurements) to the data. Then, Hanjie Pan's observation in [7] is that, in practice, the K sinusoids that have the largest amplitude are the correctly paired sinusoids.

III. ALGORITHMIC SETTING

We have sketched in Section II-B the algorithm that performs joint FRI reconstruction of multi-sensor data. We now detail our preferred implementation of these ideas.

A. Vector-FRI Algorithm Implementation

Denoting by $\mathbf{V}_{N,N'}$ the $N \times N'$ inverse DFT matrix

$$\mathbf{V}_{N,N'} = \frac{1}{N} [e^{2j\pi nn'/N}]_{\substack{0 \leq n \leq N-1 \\ 0 \leq n' \leq N'-1}}$$

the raw data of each sensor, normalized by their noise margin σ_l , are transformed into their inverse DFT:

$$\mathbf{x}_l = \mathbf{V}_{N,N} \begin{bmatrix} y_{0,l}/\sigma_l \\ y_{1,l}/\sigma_l \\ \vdots \\ y_{N-1,l}/\sigma_l \end{bmatrix} \quad (11)$$

The motivation behind the normalization is to reduce the number of iterations needed to satisfy the MSE criterion (10). Without it, if one σ_l were significantly larger than the others, there would be some chance that the criterion (6) be more efficiently decreased by just decreasing the contribution of the l -th sensor, instead of a more balanced contribution of all the sensors.

The polynomials involved in (3) can be expressed algebraically as

$$[P_{K-1,l}(e^{2j\pi n/N})]_{n=0,1,\dots,N-1} = \mathbf{V}_{N,K} \mathbf{p}_l$$

$$[Q_K(e^{2j\pi n/N})]_{n=0,1,\dots,N-1} = \mathbf{V}_{N,K+1} \mathbf{q}$$

where \mathbf{p}_l and \mathbf{q} are the coefficients of $P_{K-1,l}$ and Q_K , stacked in vector form. We further stack all the vectors \mathbf{p}_l , $l = 0, 1, \dots, L-1$ into a unique $LK \times 1$ -vector \mathbf{p} .

We assume that we have calculated an estimate \mathbf{q}^{i-1} of \mathbf{q} at iteration $i-1$. Let us denote by \mathbf{R}^{i-1} the inverse $N \times N$ diagonal matrix made of the vector $\mathbf{V}_{N,K+1} \mathbf{q}^{i-1}$ along its diagonal. Then, at iteration i , the minimization problem (6) can be reformulated as

$$\{\mathbf{p}^i, \mathbf{q}^i\} = \arg \min_{\mathbf{p}, \mathbf{q}} \|\mathbf{A}^{i-1} \mathbf{q} - \mathbf{B}^{i-1} \mathbf{p}\|^2 \quad (12)$$

where the matrices $\mathbf{A}^{i-1}, \mathbf{B}^{i-1}$ are given by (\otimes = Kronecker product)

$$\mathbf{A}^{i-1} = \begin{bmatrix} \text{diag}(\mathbf{x}_0) \\ \text{diag}(\mathbf{x}_1) \\ \vdots \\ \text{diag}(\mathbf{x}_{L-1}) \end{bmatrix} \mathbf{R}^{i-1} \mathbf{V}_{N,K+1},$$

$$\mathbf{B}^{i-1} = \mathbf{Id}_{L \times L} \otimes (\mathbf{R}^{i-1} \mathbf{V}_{N,K})$$

Notice that \mathbf{B}^{i-1} is full rank, which comes from the fact that both \mathbf{R}^{i-1} and $\mathbf{V}_{N,K}$ are full rank. In order to attain an unique solution \mathbf{q}^i to (12), a linear constraint $(\mathbf{q}^0)^H \mathbf{q}^i = 1$ is imposed,¹ where \mathbf{q}^0 is the initialization of the algorithm. With this constraint, the minimization in (12) results in the update

$$\begin{bmatrix} \mathbf{q}^i \\ -\mathbf{p}^i \end{bmatrix} = \lambda \left([\mathbf{A}^{i-1}, \mathbf{B}^{i-1}]^H [\mathbf{A}^{i-1}, \mathbf{B}^{i-1}] \right)^{-1} \begin{bmatrix} \mathbf{q}^0 \\ 0 \end{bmatrix} \quad (13)$$

where λ is such that $(\mathbf{q}^0)^H \mathbf{q}^i = 1$ is satisfied.

For each random initialization \mathbf{q}^0 , we keep iterating the polynomial coefficients \mathbf{q}^i until the MSE criterion (10) is satisfied. It is possible that the stopping criterion may not be met for certain choices of \mathbf{q}^0 after reaching the maximum iteration count = i_{\max} . In such cases, the algorithm is restarted with a different initialization. Typically, in all our (extensive) tests, 5 random initializations and $i_{\max} = 15$ have been sufficient to obtain a solution that fits our sensor data within the expected noise margins. In practice, a deterministic initialization can be obtained by evaluating the FFT spectrum of a single sensor data for which the MSE budget is the smallest—picking the K most prominent peaks (“*islocalmax*” function in Matlab), which works in the vast majority of the cases in our observation (> 90%). The main procedure is summarized in Algorithm 1.

¹This ensures experimentally (see [50]) that, after a finite number of trials (iterations and random initializations), one of the iterates is within the MSE budget. Other normalization strategies have been found to be less successful in this aspect, such as a quadratic constraint $\|\mathbf{q}\| = 1$; or a linear constraint on one component of \mathbf{q} , e.g., $\mathbf{e}_0^H \mathbf{q} = 1$, where $\mathbf{e}_0 = [1, 0, \dots, 0]^T$.

Algorithm 1: Vector-FRI Algorithm.

Input: Multi-sensor measurements $\{y_{n,l}\}_{n=0 \dots N-1}^{l=0 \dots L-1}$, noise margin $\{\sigma_l\}_{l=0 \dots L-1}$

- 1: IDFT of the normalized original data using (11)
- 2: **for** $loop = 1$ to $max. initializations$ **do**
- 3: Initialize \mathbf{q} with a random vector \mathbf{q}^0 ;
- 4: **for** $i = 1$ to $max. iterations$ **do**
- 5: Build the matrices involved in (13) with \mathbf{q}^{i-1} , such as \mathbf{A}^{i-1} , \mathbf{B}^{i-1} , and etc;
- 6: Update \mathbf{q}^i and \mathbf{p}^i by solving (13);
- 7: **if** $\sum_{n=0}^{N-1} |x_{n,l} - \frac{P_{K-1,l}(z)}{Q_K(z)}|^2 \leq N$, for all l **then**
- 8: Terminate all loops;
- 9: **end if**
- 10: **end for**
- 11: **end for**
- 12: $\mathbf{q} = \mathbf{q}^i$, $\mathbf{p} = \mathbf{p}^i$;
Calculate $\{u_k\}_{k=1 \dots K}$ and $\{c_{k,l}\}_{k=1 \dots K}^{l=0 \dots L-1}$ using (7) and (8).

Output: The frequencies $\{u_k\}_{k=1 \dots K}$ and coefficients $\{c_{k,l}\}_{k=1 \dots K}^{l=0 \dots L-1}$.

B. Model Order

As mentioned in Sec II-C, the key idea is to consider that any sum of K sinusoids that fits our sensor measurements within the given noise margins is a valid solution to our problem. Consequently, following Occam's razor principle [57], the “best” model order we choose is the smallest value of K for which this sum of sinusoids still satisfies the MSE budget criterion (10) for all the sensors. The detailed implementation of this model-order determination utilizes a dichotomous approach that was presented in [50].

IV. SIMULATION RESULTS**A. Performance Analysis**

We compare the proposed algorithm with several state-of-the-art techniques: matrix pencil [58], MUSIC [33], L_2 -based CS [39] and atomic-norm based CS [40]. We first perform assessment of the proposed algorithm in terms of the Cramér-Rao lower bounds, as seen in Fig. 3.

The evaluation of the computational cost is presented in Fig. 4. Furthermore, we test the proposed algorithm in terms of the perturbation on the input noise level, as shown in Fig. 5. In the presence of heavy noise (e.g. SNR < -10 dB), the proposed algorithm can retrieve the frequencies with large amplitude but may miss those smaller ones.

B. Joint Frequency Estimation From Multi-Sensor Data

In this subsection, we consider the joint frequency estimation from multi-sensor data with different noise levels σ_l^2 . Note that these sensors may not be of the same type (e.g. accelerometer, pressure sensor, vector particle velocity sensor, etc.). In this simulation, three sensor data are generated with SNR = 15 dB,

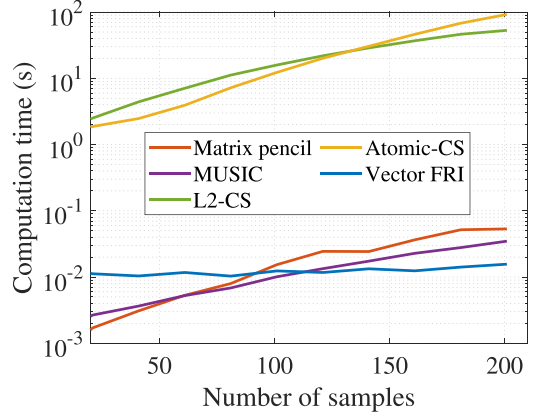


Fig. 4. Assessment of the computation time (averages over 10000 random realizations, $L = 3$ sensors and $K = 2$ sinusoids). The low computational cost of Vector-FRI allows efficient processing of large amounts of data in real-time applications.

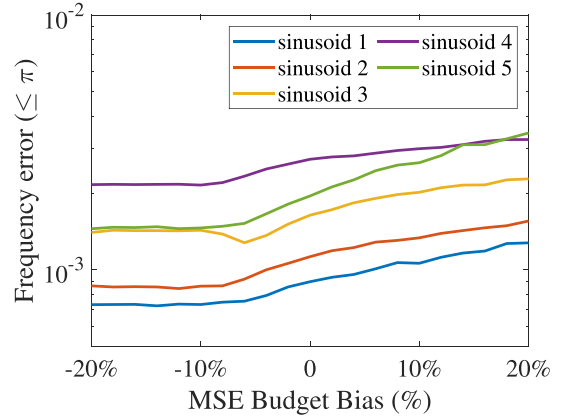


Fig. 5. Vector-FRI algorithm is robust to inaccuracy of the input MSE budget (averages over 5000 random realizations, $K = 5$ sinusoids, $N = 21$ samples and $L = 3$ sensors).

10 dB, and 5 dB (50 samples). Fig. 6 shows the results of matrix pencil, MUSIC, L_2 -based CS, atomic-norm based CS and Vector-FRI ($K = 10$ sinusoids with different amplitudes across sensors, $L = 3$ sensors). For visualization purpose, we only show the reconstruction of the frequencies.

As can be seen from Fig. 6, our Vector-FRI retrieves all frequencies accurately. Moreover, it was able to retrieve correctly the model order ($K = 10$ sinusoids here) from the knowledge of the MSE of the 3 sensors. Other high-resolution techniques (matrix pencil, MUSIC, atomic-norm based CS, L_2 -based CS, etc.) require the extra knowledge of the input number of sinusoids and struggle to resolve closely-located frequencies.

In practice, inputting more noisy sensor data to standard high-resolution techniques does not always give rise to more accurate frequency estimation. As a result, practitioners usually abandon sensor data with large MSE budget. Contrary to dropping sensor data, the proposed algorithm exploits the maximum of the multi-sensor data. As can be seen in Table I (averages over 10000 random realizations), using more sensor data provides a more accurate frequency estimation—using all three sensors leads to the best result, even if the data of Sensor 3 is quite noisy.

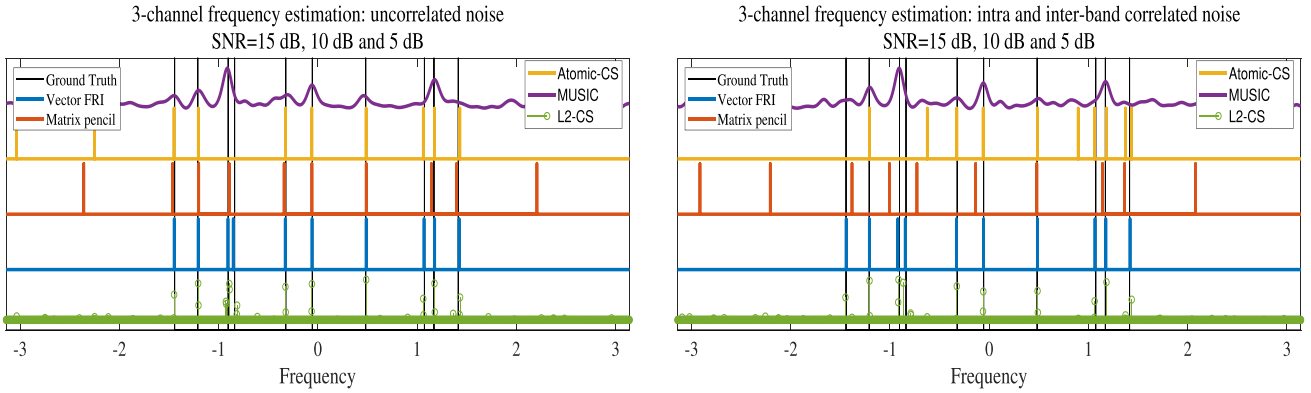


Fig. 6. Joint frequency estimation from 3-sensor data ($K = 10$ sinusoids and $N = 50$ samples) in two noise scenarios. The run-time of Vector-FRI, matrix pencil, MUSIC, L_2 -based CS, and atomic-norm based CS is 0.0105 s, 0.0088 s, 0.0196 s, 19.5329 s, and 2.0071 s. Our algorithm automatically determines the model order (see Section III-B), and achieves a very accurate frequency retrieval in all scenarios. Other techniques are less accurate when dealing with correlated noise. Moreover, in all scenarios they struggle to resolve closely-located frequencies.

TABLE I
MORE SENSORS, HIGHER ACCURACY

Data	Sensor 1	Sensor 2	Sensor 3	Sensor 1, 2	Sensor 1, 3	Sensor 2, 3	Sensor 1, 2, 3
Maximum Frequency Error	0.0710	0.8811	1.0185	0.0307	0.0359	0.5838	0.0280
Mean Frequency Error	0.0413	0.3701	0.5209	0.0199	0.0242	0.2860	0.0189

The SNRs of Sensor 1, Sensor 2, Sensor 3 are 15dB, 10dB, and 5dB (averages over 10000 random realizations, $K = 4$ sinusoids and $N = 15$ samples). The more sensors used, the higher the accuracy of the estimation results.

C. DOA Estimation for 2D Planar Array

DOA estimation is a classic problem that is frequently encountered in underwater acoustic, radioastronomy, and speech signal processing [6], [59], [9]. An uniform rectangular array (URA) with 25×21 sensors (as show in Fig. 7(a)) is used for data simulation.

For the narrowband sources, the received signals in frequency domain can be expressed as [60]

$$I(n_1, n_2) = \sum_{k=1}^K c_k e^{-j\left(\frac{2\pi\Delta d_1}{\lambda} n_1 u_{k,1} + \frac{2\pi\Delta d_2}{\lambda} n_2 u_{k,2}\right)} \quad (14)$$

where c_k is the coefficient of the k -th source. $u_{k,1} = \sin \theta_k \cos \phi_k$ and $u_{k,2} = \sin \theta_k \sin \phi_k$ are spatial frequencies related to physical azimuth ϕ_k and elevation angle θ_k , where $\Delta d_1 = 0.5\lambda$ and $\Delta d_2 = 0.5\lambda$ are the element spacing along horizontal and vertical direction, and λ is the wavelength. Therefore, the essential problem for DOA estimation is to retrieve the spatial frequency pairs $(u_{k,1}, u_{k,2})$ and the corresponding coefficients c_k .

The classical methods, e.g. CBF, MVDR, MUSIC, and CS, are to assume that the sources are located on discrete grid (i.e. gridding). In this case, the accuracy of reconstructed signal is limited by the grid step. Alternatively, we handle the DOA estimation directly with high resolution using our Vector-FRI algorithm.

We demonstrate the effectiveness of our Vector-FRI algorithm in Fig. 7(b). In this case, there are ten sources with $\text{SNR} = 20$ dB. Standard techniques (like CBF, MUSIC, etc.) fail to resolve the

closer sources because of the low resolution, and has the drawbacks of false targets due to high sidelobes. Atomic-norm based CS is not robust enough to resolve all the DOAs. By contrast, our Vector-FRI algorithm retrieves all the source locations with high accuracy and strong robustness.

V. EXPERIMENTAL RESULTS

A. Joint Frequency Estimation From SWellEx-96 Experiment

The performance of our Vector-FRI algorithm is further validated using real data collected for localization, tracking, geoacoustic inversion, measurements of ambient noise, etc in the complex shallow-water environment (see Fig. 8). The processed data set is from the shallow water evaluation cell experiment 1996 (SWellEx-96) Event S5, occurred from 23 : 15 to 0 : 30 in the west of Point Loma, CA.

During the experiment, the data is collected by a vertical linear array with 21 sensors. The array is located at a depth of 94.125 m to 212.25 m. The data we are interested in is collected at about 23 : 52 when the deep source was towed at a depth of about 54 m, transmitting numerous tonals of various source levels between 49 Hz and 400 Hz, and the shallow source was towed at a depth of about 9 m. The hydrophone measures the sensor data with a frequency band from 180 Hz to 400 Hz, which results in very intricate measurement noise that is intrinsically non-stationary, colored, and correlated. The experimental parameters are set as follows:

- 1) The vertical linear array consists of $L = 21$ sensors;

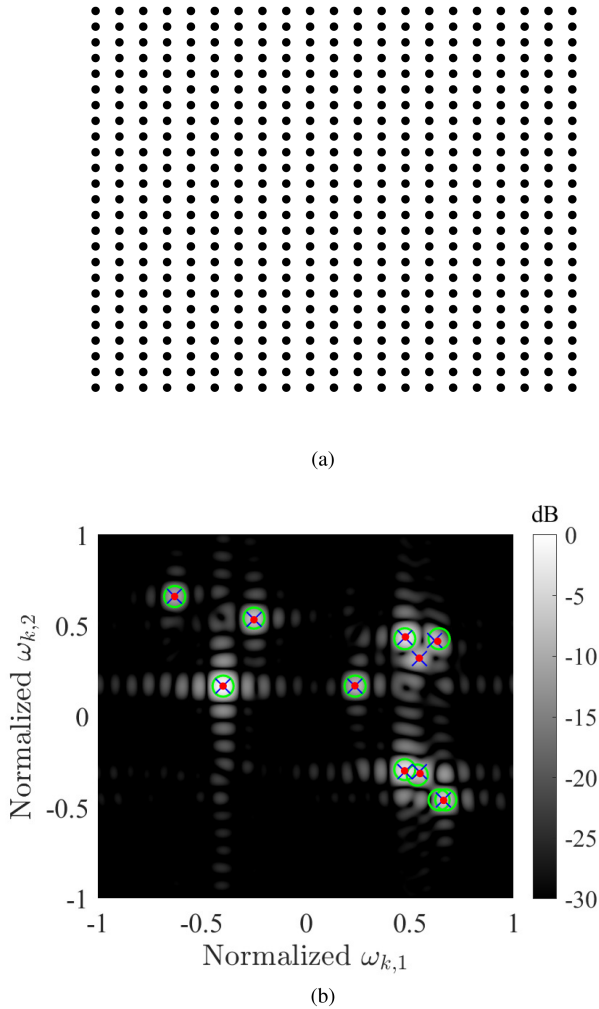


Fig. 7. DOA estimation for 2D planar array. (a) Uniform rectangular array with 25×21 sensors. (b) CBF (background color), Atomic-CS (green circles) and Vector-FRI DOA estimation (blue crosses) for 10 sources with SNR = 20 dB. Note that “●” denotes the ground truth.

- 2) The raw sensor data contains $K = 10$ frequencies [198, 201, 232, 235, 280, 283, 335, 338, 385, 388] Hz;
- 3) The sampling time is 0.25 s with the sampling frequency of 1500 Hz, i.e. $N = 375$ samples;
- 4) The MSE budget is obtained from pre-measurements when there is no source in the observation area (see Table III in Supplementary Materials).

Since the actual marine environment is complex and time-varying due to the influence of waves [61], tides [62] and currents [63] (these also lead to acoustic disturbances and colored noise), it is difficult and expensive to collect acoustic signals, e.g. expensive equipment (several hundred thousand dollars) and charter fee (tens of thousands of dollars a day), and difficult deployment and recycling (bad weather, turbulent water, and difficult underwater operations). Therefore, it is of great significance to accurately estimate the frequency in a short time. To further test the performance of our algorithm, a short-time set of samples with a duration of 0.25 s (sampling frequency 1500 Hz) are selected. Notably, the associated amplitudes are

unknown due to the frequency selectivity in the ocean, so they are displayed as lines.

As shown in Fig. 8(b) and (c), our Vector-FRI can resolve all frequencies successfully and provide an exact K -sparsity recovery. Standard sub-space based high-resolution techniques like MUSIC cannot provide sufficient resolution and robustness, leading to failures to resolve closely located frequencies. CS fails to retrieve the frequencies with poor sparsity and limited resolution. The essential reason is that, in real data collection, the actual measurement noise is very sophisticated (non-white, correlated, and non-stationary), which is caused by measuring environmental changes and instrument precision [25], [26], [42], [43].

In this section, our Vector-FRI algorithm achieves accurate recovery using fewer samples in the presence of intricate measurement noise ($N = 375$ samples). And that is important in practical applications, such as real-time communications and tracking, where common techniques in practice usually require a long sampling time (typically, equivalent to 4500 samples) and high computational cost. It allows us to acquire the real data with a much lower cost on sampling and transmission, and improve the resolution on frequency estimation, which significantly broadens the scope of application.

B. Interference Fringes Reconstruction in Underwater Acoustics

The underwater acoustic intensity of a broadband signal usually exhibits a regular stripe pattern (see Fig. 10(a)) in the frequency-range domain, whose parallel slope geometry implicitly contains the information of the environment and the sound source [64]. The pattern can be utilized to promote many practical applications, e.g. ranging from sound source localization [65], array data processing [66], time-reversal focusing [67], and geoacoustic inversion [68], [69]. However, The actual data contains a lot of disturbances because of the complicated sea environment e.g. internal soliton waves (ISWs) propagate between sound source and receivers (see Fig. 9). And this greatly limits the measurement and application of slope geometry, so it is necessary to develop a robust method to retrieve the slope geometry (direction) of stripe pattern [70].

In fact, the acoustic signal propagates in specific modes (normal modes) due to the waveguide environment [71]. Therefore, an acoustic stripe pattern can be considered as the combination of normal mode pairs with the similar direction. The regular pattern an obvious direction can be regarded as

$$I(\mathbf{r}) = g(\mathbf{u}^\top \mathbf{r}), \quad \text{where } \|\mathbf{u}\| = 1 \quad (15)$$

where \mathbf{r} is the coordinate vector of the pattern, g is the generator function of the interference pattern, and g is empirically not sparse whose Fourier spectrum has several finite support band centered at certain frequencies. g depends on many factors, e.g. sound speed profile and water depth. In this section, we are more interested in $\mathbf{u} = [\cos \alpha, \sin \alpha]^\top$, who characterizes the (slope) of the interference pattern, and it is closely related to the location of the sound source [65]. α is the angle between

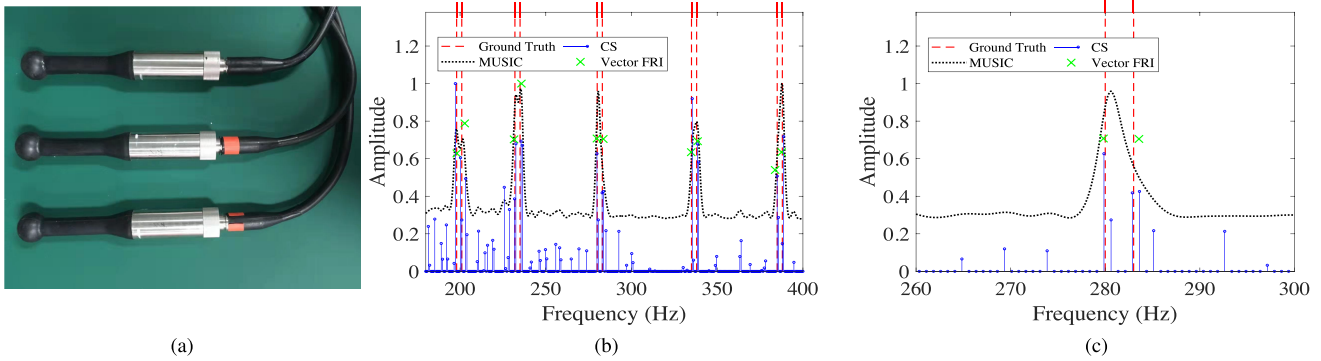


Fig. 8. Comprehensive shallow-water environment experiments: the goal is to retrieve multiple closely located source frequencies (with unknown amplitudes) at [198, 201, 232, 235, 280, 283, 335, 338, 385, 388] Hz. (a) Hydrophones. (b) The frequency estimation results of Vector-FRI, MUSIC, and CS from 21-sensor data. The run-time of Vector-FRI, MUSIC and CS is 0.3290 s, 0.2205 s and 17831 s. Our algorithm is 54200 times faster than compressive sensing (CS). (c) The zoomed figure of (b). Our algorithm achieves a high-quality recovery that accurately retrieves all frequencies, whereas standard high-resolution techniques (MUSIC, compressive sensing) cannot process these data due to sophisticated noise (correlated, colored, non-stationary).

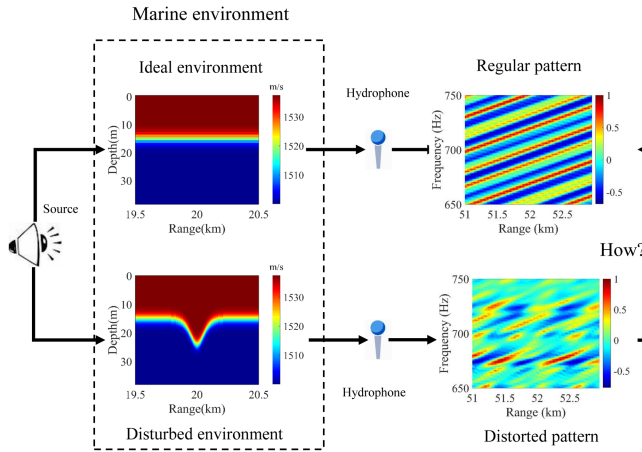


Fig. 9. Illustration of acoustic intensity interferogram measurements. The acoustic intensity interferogram appears as regular stripes in the ideal environment (the range-independent sound speed profile). But the regular stripes are damaged in the disturbed environment (the range-dependent sound speed profile caused by ISWs). Our goal is to recover the directionality of the regular pattern from the distorted pattern.

the pattern direction and the horizontal direction. However, the regular directionality can be buried by interference due to ISWs (occurs frequently in the ocean) [61]. And traditional methods, e.g. 2D DFT and 2D MUSIC, cannot solve this problem [71] and fail to resolve the ground truth from the interference with insufficient resolution.

Fig. 9 shows the illustration of acoustic intensity interferogram measurements. Our goal is to recover the directionality of the regular pattern from the distorted pattern. The experimental settings are as follows. A point source with the frequency band of [650 : 2 : 750] Hz is located at a depth of 35 m. The horizontal line array is also at a depth of 35 m, ranging from 51 km to 53 km with a spacing of 50 m. And the depth of water is 38 m. The experimental parameters are set as follows:

- 1) The size of fringes pattern is 51×41 with $\alpha = 117.88^\circ$;

- 2) The regular pattern contains $K = 3$ pairs of 2D sinusoids (see Fig. 10);
- 3) The MSE budget is set to 0, which means running the algorithm for a fixed number of iterations and initializations and choosing the reconstruction that yields the minimum MSE.

Fig. 10(a) indicates the received acoustic intensity without ISWs in the range-frequency domain. There are clear and regular interference fringes whose direction contains useful information ($\alpha = 117.88^\circ$). The 2D DFT of the regular pattern in Fig. 10(b) reveals three principal frequency pair components (regarded as ground truth), which actually corresponds to mode pairs (1,2), (2,3), and (1,3), respectively and they determine the direction of the pattern. In fact, although this pattern is not absolutely sparse, the sparse approximation is sufficient for direction. Fig. 10(c) shows the results of sparse approximation without ISWs ($\alpha = 117.94^\circ$). The parallel slope geometry of acoustic intensity is completely preserved compared with Fig. 10(a), which also shows the effectiveness of sparse approximation.

When ISWs occur, the regular pattern is damaged due to the propagation of ISWs [70], [71] (see Fig. 10(d)). Subsequently, the distorted pattern contains many additional frequency (direction) components caused by the coupling of different modes (see Fig. 10(e)). In this case, the effective direction information is buried by lots of interference and is difficult to obtain.

Fortunately, the original frequency (direction) components (corresponding to uncoupled mode pairs) in Fig. 10(b) are always invariant across the period of ISWs according to the mode-coupling theory, but the additional frequency components (coupled-mode pairs) varies with the location of ISWs [71]. Therefore, the original invariant frequencies can be distinguished from the dirty frequency components as shown in Fig. 10(e). The reconstructed pattern using the three original frequency components (uncoupled modes) are indicated in Fig. 10(f). It still retains the regular structure (valid information, $\alpha = 117.19^\circ$) in the the original pattern in Fig. 10(a). That is to

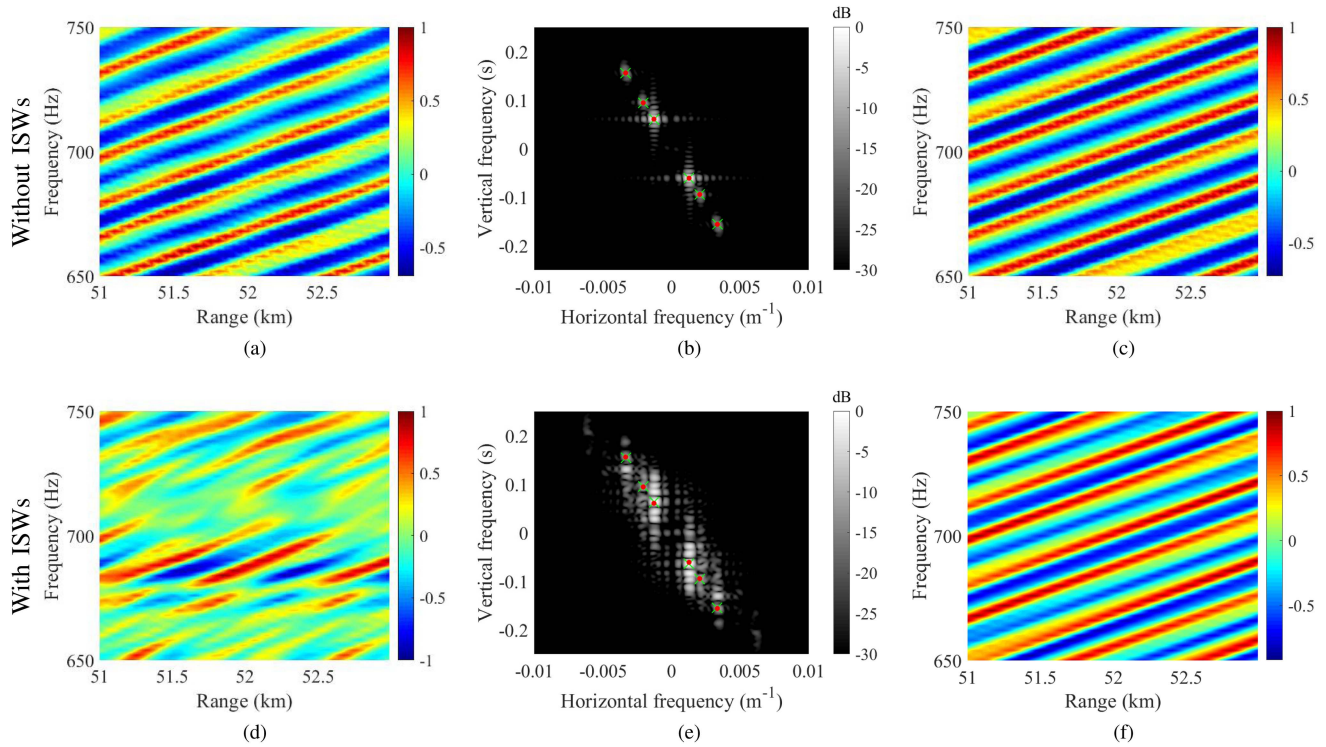


Fig. 10. Interference fringes reconstruction of underwater acoustic intensity. (a) Interference fringes of acoustic intensity without disturbance ($\alpha = 117.88^\circ$). (b) The 2D frequency spectrum of (a). Background color represents the 2D DFT, • denotes the ground truth (uncoupled-mode pairs), \times denotes the results of Vector-FRI. (c) The 2D sparse approximation of interference fringes using Vector-FRI without disturbance ($\alpha = 117.94^\circ$). (d) The distorted interference fringe pattern is caused by disturbance. (e) The 2D frequency spectrum of the distorted pattern is calculated by 2D DFT (background color) and Vector-FRI with disturbance. (f) The reconstructed pattern ($\alpha = 117.19^\circ$) using Vector-FRI.

say, our Vector-FRI algorithm provides an accurate estimation for the direction of acoustic fringes in underwater.

VI. CONCLUSION

Motivated by the requirements of multi-sensor applications, we propose a Vector-FRI (finite rate of innovation) framework for the joint sparse recovery of multi-sensor measurements, which can be viewed as a collection of 1D sinusoidal samples with the same frequencies, but different amplitudes. We demonstrate that robust recovery can be achieved by fitting the multi-sensor data to the joint parametric model, even if the instrument precision is non-uniform and noise is correlated. Instead of minimizing the model-fitting error, our key idea is to consider any K -sinusoidal approximation that fits the multi-sensor data within a given noise margin (MSE budget) is a valid solution to our problem: our fitted parametric representation is as close (or closer) to the noisy data as the underlying ground-truth is.

Moreover, we point out that the noise margin and the order of the parametric model are interdependent: given a pre-defined noise margin, the order of the model is the smallest number of innovations/sinusoids for which this sum is still a valid solution; on the other hand, if we fix the model order, the smallest MSE attained by our algorithm (15 iterations for 5 random initialization) provides an estimate of the noise margin that characterizes the inaccuracy of each sensor data.

In practice, we demonstrate that our method can be easily extended to multi-dimensional sensor measurements and provides a generic strategy for many practical applications, e.g. direction-of-arrival data of 2D planar array, optical interferometric image, and interference fringes of underwater acoustics. We develop a very efficient and robust algorithm and validate it through various simulations and multiple types of real data.

ACKNOWLEDGMENT

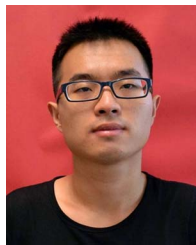
The authors would like to thank Yongsung Park for providing the atomic-CS code in simulations.

REFERENCES

- [1] N. P. Grets and J. D. Kasarda, "Enterprise logistics in the information era," *California Manage. Rev.*, vol. 39, no. 4, pp. 55–78, 1997.
- [2] B. Lafferty, R. Quinn, and C. Breen, "A side-scan sonar and high-resolution chirp sub-bottom profile study of the natural and anthropogenic sedimentary record of lower lough erne, northwestern Ireland," *J. Archaeological Sci.*, vol. 33, no. 6, pp. 756–766, 2006.
- [3] T. Blu, P.-L. Dragotti, M. Vetterli, P. Marziliano, and L. Coulot, "Sparse sampling of signal innovations," *IEEE Signal Process. Mag.*, vol. 25, no. 2, pp. 31–40, Mar. 2008.
- [4] M. Vetterli, P. Marziliano, and T. Blu, "Sampling signals with finite rate of innovation," *IEEE Trans. Signal Process.*, vol. 50, no. 6, pp. 1417–1428, Jun. 2002.
- [5] R. Guo and T. Blu, "FRI sensing: Sampling images along unknown curves," in *Proc. IEEE Int. Conf. Acoust., Speech Signal Process.*, 2019, pp. 5132–5136.

- [6] Y. Li, R. Guo, T. Blu, and H. Zhao, "Generic FRI-based DOA estimation: A model-fitting method," *IEEE Trans. Signal Process.*, vol. 69, pp. 4102–4115, 2021.
- [7] H. Pan, T. Blu, and M. Vetterli, "Towards generalized FRI sampling with an application to source resolution in radioastronomy," *IEEE Trans. Signal Process.*, vol. 65, no. 4, pp. 821–835, Feb. 2017.
- [8] R. Guo and T. Blu, "FRI sensing: Retrieving the trajectory of a mobile sensor from its temporal samples," *IEEE Trans. Signal Process.*, vol. 68, pp. 5533–5545, 2020.
- [9] F.-M. Hoffmann, P. A. Nelson, and F. M. Fazi, "DOA estimation performance with circular arrays in sound fields with finite rate of innovation," *IEEE/ACM Trans. Audio, Speech, Lang. Process.*, vol. 28, pp. 171–184, 2019.
- [10] F. Bellili, S. Affes, and A. Stéphenne, "DOA estimation for ULA systems from short data snapshots: An annihilating filter approach," in *Proc. IEEE Glob. Telecommun. Conf.*, 2011, pp. 1–5.
- [11] R. Guo and T. Blu, "Exploring the geometry of one-dimensional signals," *IEEE Trans. Signal Process.*, vol. 69, pp. 5299–5312, 2021.
- [12] S. Rudresh and C. S. Seelamantula, "Finite-rate-of-innovation-sampling-based super-resolution radar imaging," *IEEE Trans. Signal Process.*, vol. 65, no. 19, pp. 5021–5033, Oct. 2017.
- [13] T. K. Sarkar and O. Pereira, "Using the matrix pencil method to estimate the parameters of a sum of complex exponentials," *IEEE Antennas Propag. Mag.*, vol. 37, no. 1, pp. 48–55, Feb. 1995.
- [14] J. A. Cadzow, "Signal enhancement—A composite property mapping algorithm," *IEEE Trans. Acoust., Speech, Signal Process.*, vol. 36, no. 1, pp. 49–62, Jan. 1988.
- [15] S. M. Kay, *Modern Spectral Estimation: Theory and Application*. Englewood Cliffs, NJ, USA: Prentice Hall, 1988.
- [16] R. P. Millane, "Phase retrieval in crystallography and optics," *J. Opt. Soc. America*, vol. 7, no. 3, pp. 394–411, 1990.
- [17] A. R. Thompson, J. M. Moran, and G. W. Swenson, *Interferometry and Synthesis in Radio Astronomy*. Berlin, Germany: Springer, 2017.
- [18] M. Mundt et al., "Assessment of the measurement accuracy of inertial sensors during different tasks of daily living," *J. Biomech.*, vol. 84, pp. 81–86, 2019.
- [19] E. Sertel, S. Kutoglu, and S. Kaya, "Geometric correction accuracy of different satellite sensor images: Application of figure condition," *Int. J. Remote Sens.*, vol. 28, no. 20, pp. 4685–4692, 2007.
- [20] H. Wen, Z. Xiao, A. Markham, and N. Trigoni, "Accuracy estimation for sensor systems," *IEEE Trans. Mobile Comput.*, vol. 14, no. 7, pp. 1330–1343, Jul. 2015.
- [21] Y. Wu, C. Hou, G. Liao, and Q. Guo, "Direction-of-arrival estimation in the presence of unknown nonuniform noise fields," *IEEE J. Ocean. Eng.*, vol. 31, no. 2, pp. 504–510, Apr. 2006.
- [22] M. A. Pimentel, M. D. Santos, C. Arteta, J. S. Domingos, M. A. Maraci, and G. D. Clifford, "Respiratory rate estimation from the oscillometric waveform obtained from a non-invasive cuff-based blood pressure device," in *Proc. IEEE 36th Annu. Int. Conf. IEEE Eng. Med. Biol. Soc.*, 2014, pp. 3821–3824.
- [23] F. Landreani et al., "Respiratory frequency estimation from accelerometric signals acquired by mobile phone in a controlled breathing protocol," in *Proc. IEEE Comput. Cardiol.*, 2017, pp. 1–4.
- [24] W. Karlen, S. Raman, J. M. Ansermino, and G. A. Dumont, "Multiparameter respiratory rate estimation from the photoplethysmogram," *IEEE Trans. Biomed. Eng.*, vol. 60, no. 7, pp. 1946–1953, Jul. 2013.
- [25] T. Nagayama, A. Rekswardojo, D. Su, and T. Mizutani, "Bridge natural frequency estimation by extracting the common vibration component from the responses of two vehicles," *Eng. Struct.*, vol. 150, pp. 821–829, 2017.
- [26] J. D. Sitton, D. Rajan, and B. A. Story, "Bridge frequency estimation strategies using smartphones," *J. Civil Struct. Health Monit.*, vol. 10, no. 3, pp. 513–526, 2020.
- [27] J. P. Lynch and K. J. Loh, "A summary review of wireless sensors and sensor networks for structural health monitoring," *Shock Vib. Dig.*, vol. 38, no. 2, pp. 91–130, 2006.
- [28] Q. Kong, R. M. Allen, M. D. Kohler, T. H. Heaton, and J. Bunn, "Structural health monitoring of buildings using smartphone sensors," *Seismological Res. Lett.*, vol. 89, no. 2A, pp. 594–602, 2018.
- [29] A. Moreno-Gomez, C. A. Perez-Ramirez, A. Dominguez-Gonzalez, M. Valtierra-Rodriguez, O. Chavez-Alegria, and J. P. Amezquita-Sanchez, "Sensors used in structural health monitoring," *Arch. Comput. Methods Eng.*, vol. 25, no. 4, pp. 901–918, 2018.
- [30] H. B. Mitchell, *Multi-Sensor Data Fusion: An Introduction*. Berlin, Germany: Springer, 2007.
- [31] J. Dong, D. Zhuang, Y. Huang, and J. Fu, "Advances in multi-sensor data fusion: Algorithms and applications," *Sensors*, vol. 9, no. 10, pp. 7771–7784, 2009.
- [32] J.-M. Papy, L. De Lathauwer, and S. V. Huffel, "Common pole estimation in multi-channel exponential data modeling," *Signal Process.*, vol. 86, no. 4, pp. 846–858, 2006.
- [33] R. Schmidt, "Multiple emitter location and signal parameter estimation," *IEEE Trans. Antennas Propag.*, vol. AP-34, no. 3, pp. 276–280, Mar. 1986.
- [34] P. Gerstoft, A. Xenaki, and C. F. Mecklenbräuker, "Multiple and single snapshot compressive beamforming," *J. Acoust. Soc. Amer.*, vol. 138, no. 4, pp. 2003–2014, 2015.
- [35] N. Yilmazer, T. K. Sarkar, and M. Salazar-Palma, "DOA estimation using matrix pencil and esprit methods using single and multiple snapshots," in *Proc. IEEE URSI Int. Symp. Electromagn. Theory*, 2010, pp. 215–218.
- [36] N. Yilmazer, S. Ari, and T. K. Sarkar, "Multiple snapshot direct data domain approach and esprit method for direction of arrival estimation," *Digit. Signal Process.*, vol. 18, no. 4, pp. 561–567, 2008.
- [37] M. F. Khan and M. Tufail, "Multiple snapshot beamspace matrix pencil method for direction of arrival estimation," in *Proc. IEEE 2nd Int. Conf. Ind. Mechatronics Automat.*, 2010, vol. 2, pp. 288–291.
- [38] N. Dharamdial, R. Adve, and R. Farha, "Multipath delay estimations using matrix pencil," in *Proc. IEEE Wireless Commun. Netw.*, 2003, pp. 632–635.
- [39] A. Xenaki, P. Gerstoft, and K. Mosegaard, "Compressive beamforming," *J. Acoust. Soc. Amer.*, vol. 136, no. 1, pp. 260–271, 2014.
- [40] Y. Park, Y. Choo, and W. Seong, "Multiple snapshot grid free compressive beamforming," *J. Acoust. Soc. Amer.*, vol. 143, no. 6, pp. 3849–3859, 2018.
- [41] Z. Dou, C. Shi, Y. Lin, and W. Li, "Modeling of non-Gaussian colored noise and application in CR multi-sensor networks," *EURASIP J. Wireless Commun. Netw.*, vol. 2017, no. 1, pp. 1–11, 2017.
- [42] M. Li and Y. Lu, "Maximum likelihood DOA estimation in unknown colored noise fields," *IEEE Trans. Aerosp. Electron. Syst.*, vol. 44, no. 3, pp. 1079–1090, Jul. 2008.
- [43] S. Yazdkhasti and J. Z. Sasiadek, "Multi sensor fusion based on adaptive kalman filtering," in *Advances in Aerospace Guidance, Navigation and Control*. Berlin, Germany: Springer, 2018, pp. 317–333.
- [44] L. Miaylova, D. Angelova, D. Bull, and N. Canagarajah, "Localization of mobile nodes in wireless networks with correlated in time measurement noise," *IEEE Trans. Mobile Comput.*, vol. 10, no. 1, pp. 44–53, Jan. 2011.
- [45] P. Elias et al., "A method for minimising of low frequency and unwrapping artefacts from interferometric calculations," *Int. J. Remote Sens.*, vol. 27, no. 14, pp. 3079–3086, 2006.
- [46] J. Gao, Y. Qin, B. Deng, H. Wang, and X. Li, "A novel method for 3-D millimeter-wave holographic reconstruction based on frequency interferometry techniques," *IEEE Trans. Microw. Theory Techn.*, vol. 66, no. 3, pp. 1579–1596, Mar. 2018.
- [47] J.-I. Kato, I. Yamaguchi, T. Nakamura, and S. Kuwashima, "Video-rate fringe analyzer based on phase-shifting electronic moiré patterns," *Appl. Opt.*, vol. 36, no. 32, pp. 8403–8412, 1997.
- [48] E. Sánchez-Ortiga, A. Doblas, G. Saavedra, M. Martínez-Corral, and J. García-Sucerquia, "Off-axis digital holographic microscopy: Practical design parameters for operating at diffraction limit," *Appl. Opt.*, vol. 53, no. 10, pp. 2058–2066, 2014.
- [49] C. Gilliam and T. Blu, "Fitting instead of annihilation: Improved recovery of noisy FRI signals," in *Proc. IEEE Int. Conf. Acoust., Speech Signal Process.*, 2014, pp. 51–55.
- [50] C. Gilliam and T. Blu, "Finding the minimum rate of innovation in the presence of noise," in *Proc. IEEE Int. Conf. Acoust., Speech Signal Process.*, 2016, pp. 4019–4023.
- [51] R. Guo and T. Blu, "FRI sensing: 2D localization from 1D mobile sensor data," in *Proc. IEEE Asia-Pacific Signal Inf. Process. Assoc. Annu. Summit Conf.*, 2020, pp. 986–991.
- [52] R. Prony, "Essai experimental--," *J. de l'Ecole Polytechnique*, vol. 2, 1795, Art. no. 929.
- [53] P. Stoica and R. L. Moses, "Spectral analysis of signals," 2005.
- [54] C. Sanathanan and J. Koerner, "Transfer function synthesis as a ratio of two complex polynomials," *IEEE Trans. Autom. Control*, vol. AC-8, no. 1, pp. 56–58, Jan. 1963.
- [55] K. Steiglitz and L. McBride, "A technique for the identification of linear systems," *IEEE Trans. Autom. Control*, vol. AC-10, no. 4, pp. 461–464, Oct. 1965.
- [56] S.-W. Park and A. Kattianon, "Accurate frequency estimation using SVD method and steiglitz-mcbride algorithm," in *Proc. IEEE 4th Int. Conf. Signal Process. (Cat. No. 98TH8344)*, 1998, pp. 172–175.

- [57] C. E. Rasmussen and Z. Ghahramani, "Occam's razor," in *Proc. Adv. Neural Inf. Process. Syst.*, 2001, pp. 294–300.
- [58] Y. Hua and T. Sarkar, "Matrix pencil method for estimating parameters of exponentially damped/undamped sinusoids in noise," *IEEE Trans. Acoust., Speech, Signal Process.*, vol. 38, no. 5, pp. 814–824, May 1990.
- [59] T. C. Yang, "Deconvolved conventional beamforming for a horizontal line array," *IEEE J. Ocean. Eng.*, vol. 43, no. 1, pp. 160–172, Jan. 2018.
- [60] P. Heidenreich, A. M. Zoubir, and M. Rubsamen, "Joint 2-D DOA estimation and phase calibration for uniform rectangular arrays," *IEEE Trans. Signal Process.*, vol. 60, no. 9, pp. 4683–4693, Sep. 2012.
- [61] S. Finette et al., "Acoustic field variability induced by time evolving internal wave fields," *J. Acoust. Soc. Amer.*, vol. 108, no. 3, pp. 957–972, 2000.
- [62] J. F. Lynch et al., "Acoustic travel-time perturbations due to shallow-water internal waves and internal tides in the barents sea polar front: Theory and experiment," *J. Acoust. Soc. Amer.*, vol. 99, no. 2, pp. 803–821, 1996.
- [63] K. G. Sabra and D. R. Dowling, "Effect of ocean currents on the performance of a time-reversing array in shallow water," *J. Acoust. Soc. Amer.*, vol. 114, no. 6, pp. 3125–3135, 2003.
- [64] D. Rouseff, "Effect of shallow water internal waves on ocean acoustic striation patterns," *Waves Random Media*, vol. 11, no. 4, 2001, Art. no. 377.
- [65] K. L. Cockrell and H. Schmidt, "Robust passive range estimation using the waveguide invariant," *J. Acoust. Soc. Amer.*, vol. 127, no. 5, pp. 2780–2789, 2010.
- [66] H. Tao and J. L. Krolik, "Waveguide invariant focusing for broadband beamforming in an oceanic waveguide," *J. Acoust. Soc. Amer.*, vol. 123, no. 3, pp. 1338–1346, 2008.
- [67] S. Kim, W. Kuperman, W. Hodgkiss, H. Song, G. Edelmann, and T. Akal, "Robust time reversal focusing in the ocean," *J. Acoust. Soc. Amer.*, vol. 114, no. 1, pp. 145–157, 2003.
- [68] Q.-Y. Ren and J.-P. Hermand, "Acoustic interferometry for geoacoustic characterization in a soft-layered sediment environment," *J. Acoust. Soc. Amer.*, vol. 133, no. 1, pp. 82–93, 2013.
- [69] K. Heaney, "Rapid geoacoustic characterization using a surface ship of opportunity," *IEEE J. Ocean. Eng.*, vol. 29, no. 1, pp. 88–99, Jan. 2004.
- [70] X. Li, W. Song, D. Gao, W. Gao, and H. Wang, "Training a U-Net based on a random mode-coupling matrix model to recover acoustic interference striations," *J. Acoust. Soc. Amer.*, vol. 147, no. 4, pp. EL363–EL369, 2020.
- [71] W. Song, N. Wang, D. Gao, H. Wang, T. Hu, and S. Guo, "The influence of mode coupling on waveguide invariant," *J. Acoust. Soc. Amer.*, vol. 142, no. 4, pp. 1848–1857, 2017.



Ruiming Guo received the B.E. degree in electronic engineering from Sichuan University, Chengdu, China, in 2017, and the Ph.D. degree from the Department of Electronic Engineering, The Chinese University of Hong Kong, Hong Kong, in 2021. He is currently a Postdoctoral Research Fellow with the Chinese University of Hong Kong, supervised by Prof. Thierry Blu. His research interests include FRI theory, FRI Sensing, sampling theory, computational imaging, non-convex optimisation, image, and signal processing. He was the recipient of the Postgraduate Student Research Excellence Awards from the Department of the Electronic Engineering, Chinese University of Hong Kong, in 2022.



Yongfei Li received the B.E. degree in electronic engineering from Sichuan University, Chengdu, China, in 2017. He is currently working toward the Ph.D. degree with the College of Information Science & Electronic Engineering, Zhejiang University, Hangzhou, China. His research interests include DOA estimation and signal processing.



Thierry Blu (Fellow, IEEE) was born in Orléans, France, in 1964. He received the Diplôme d'ingénieur from École Polytechnique, Palaiseau, France, and from Télécom Paris (ENST), Paris, France, in 1986 and 1988, respectively, and the Ph.D. degree in electrical engineering from ENST for a study on iterated rational filterbanks, applied to wideband audio coding. From 1998 and 2007, he was with the Biomedical Imaging Group, Swiss Federal Institute of Technology, Lausanne, Switzerland. He is currently a Professor with the Department of Electronic Engineering, The Chinese University of Hong Kong, Hong Kong. His research interests include wavelets, approximation and sampling theory, sparse representations, image denoising, biomedical imaging, optics, and wave propagation. Dr. Blu was the recipient of two best paper awards from the IEEE Signal Processing Society from 2003 and 2006. He is also the coauthor of a paper that was the recipient of the Young Author Best Paper Award in 2009 from the same society. He is a Member of the IEEE Signal Processing Theory and Methods Technical Committee during 2008–2013, an Associate Editor for the IEEE TRANSACTIONS ON IMAGE PROCESSING during 2002–2006, the IEEE TRANSACTIONS ON SIGNAL PROCESSING during 2006–2010, and Elsevier Signal Processing during 2008–2011. He is currently on the board of EURASIP Journal on Image and Video Processing, SIAM Journal on Imaging Sciences, and a Member of the IEEE Bio Imaging and Signal Processing Technical Committee.



Hangfang Zhao received the B.E. degree in electronic engineering from Xidian University, Xi'an, China, in 1991, the M.E. degree in underwater engineering from Harbin Engineering University, Harbin, China, in 1997, and the Ph.D. degree in communication and information systems from Zhejiang University, Hangzhou, China, in 2010. From 1991 to 2012, she was with the Hangzhou Applied Acoustics Research Institute, Hangzhou, China, where she conducted research in acoustic signal processing and acoustic engineering. In 2012, she joined Zhejiang University, where she is currently a Professor with the Department of Information Science and Electronic Engineering. Her research interests include array signal processing, acoustic tomography and acoustic imaging, and robust signal processing in uncertain environments.